

# Bayesian Analysis of the Phase II IASC–ASCE Structural Health Monitoring Experimental Benchmark Data

J. Ching, A.M.ASCE,<sup>1</sup> and J. L. Beck, M.ASCE<sup>2</sup>

**Abstract:** A two-step probabilistic structural health monitoring approach is used to analyze the Phase II experimental benchmark studies sponsored by the IASC–ASCE Task Group on Structural Health Monitoring. This study involves damage detection and assessment of the test structure using experimental data generated by hammer impact and ambient vibrations. The two-step approach involves modal identification followed by damage assessment using the pre- and post-damage modal parameters based on the Bayesian updating methodology. An Expectation–Maximization algorithm is proposed to find the most probable values of the parameters. It is shown that the brace damage can be successfully detected and assessed from either the hammer or ambient vibration data. The connection damage is much more difficult to reliably detect and assess because the identified modal parameters are less sensitive to connection damage, allowing the modeling errors to have more influence on the results.

**DOI:** 10.1061/(ASCE)0733-9399(2004)130:10(1233)

**CE Database subject headings:** Damage assessment; Bayesian analysis; Identification; Bench marks; Structural analysis; Modal analysis.

## Introduction

Structural health monitoring (SHM) techniques (e.g., Natke and Yao 1988; Hjelmstad and Shin 1997; Sanayei et al. 1999; Vanik et al. 2000; Beck et al. 2001; Chang 2001; Bernal 2002; Casciati 2002) are methodologies that use measured response to detect and locate damage in structures and quantitatively assess its severity. In recent years, civil engineers have paid much attention to SHM techniques since they have the potential to monitor the safety of civil infrastructures. The basic idea is to detect and assess damage by inferring change in structural properties from measured structural response before and after a severe loading event, e.g., from an earthquake, or by continual monitoring for long-term deterioration. Numerous SHM techniques have been developed, but there is a difficulty of comparing the merits of different techniques. In view of this situation, a series of benchmark studies were sponsored by the International Association for Structural Control (IASC)–ASCE Task Group on Structural Health Monitoring, beginning with a relatively simple benchmark problem and proceeding on to more realistic problems, to provide a common basis for comparison of different techniques (see Dyke 1999).

The benchmark studies currently consist of Phases I and II

simulated and experimental benchmark problems. The benchmark structure is a four-story, two-bay by two-bay steel-frame scale-model structure built in the Earthquake Engineering Research Laboratory at the Univ. of British Columbia, Canada. A diagram for the analytical model for the benchmark structure is shown in Fig. 1, giving dimensions and coordinate directions in which the  $x$  direction is the strong direction of the columns. The January 2004 issue of the *Journal of Engineering Mechanics* contains the results of six different studies of the Phase I simulated benchmark problems, together with a definition and overview paper (Johnson et al. 2004). Conference papers have also appeared on Phase I of the experimental benchmark (e.g., Dyke et al. 2001) and Phase II of the simulated benchmark (e.g., Bernal et al. 2002; Ching and Beck 2003b, c).

This paper focuses on Phase II of the experimental benchmark studies. Due to some issues with the data for the experimental Phase I benchmark, further tests were performed on the benchmark structure in August 2002 to gather higher quality and more extensive data. Various damage configurations were investigated by removing bracing and loosening beam–column connections within the test structure. These tests are the basis of the experimental Phase II benchmark (Dyke et al. 2003).

## Experimental Phase II Benchmark

Experimental Phase II benchmark consists of nine configurations, in which Configs. 1–6 are braced cases with Config. 1 being the reference (undamaged) case, and Configs. 7–9 are unbraced cases with Config. 7 as the reference case. For the braced cases, damage is simulated by removing braces while in the unbraced cases, damage consists of loss of rotational stiffness of some beam–column connections. In all configurations, the center of mass of each floor deviates slightly from the geometrical center of the floor to simulate typical situations in real buildings. Five damage cases are considered for the braced structure: (1) Config. 2: removal of all braces on the  $-y$  face (the face whose outward normal is the  $-y$  direction in Fig. 1); (2) Config 3: removal of the

<sup>1</sup>George W. Housner Research Fellow, Dept. of Civil Engineering, Mail Code 104-44, California Institute of Technology, Pasadena, CA 91125 (Corresponding author). E-mail: jyching@gmail.com

<sup>2</sup>Professor, Dept. of Applied Mechanics and Civil Engineering, Mail Code 104-44, California Institute of Technology, Pasadena, CA 91125. E-mail: jimbeck@caltech.edu

Note. Associate Editor: Roger G. Ghanem. Discussion open until March 1, 2005. Separate discussions must be submitted for individual papers. To extend the closing date by one month, a written request must be filed with the ASCE Managing Editor. The manuscript for this paper was submitted for review and possible publication on July 28, 2003; approved on November 14, 2003. This paper is part of the *Journal of Engineering Mechanics*, Vol. 130, No. 10, October 1, 2004. ©ASCE, ISSN 0733-9399/2004/10-1233-1244/\$18.00.

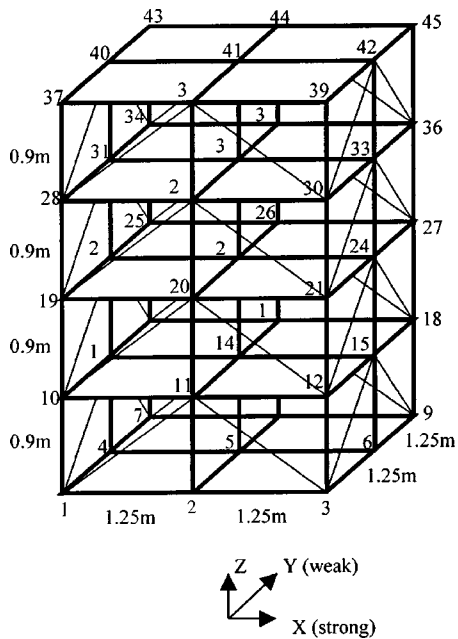


Fig. 1. Diagram of benchmark structure

left-hand-side brace in each story on the  $-y$  face in Fig. 1; (3) Config. 4: removal of the left-hand-side brace in the first and fourth stories on the  $-y$  face; (4) Config. 5: removal of the left-hand-side brace in the first story on the  $-y$  face; (5) Config. 6: removal of two braces in the second story on the  $+x$  face. Two damage cases are considered for the unbraced case: (1) Config. 8: loosen both ends of the right-hand-side beam at each floor on the  $-y$  face in Fig. 1; (2) Config. 9: loosen both ends of the right-hand-side beam at the first and second floors on the  $-y$  face.

For each configuration, experimental data were generated by three types of excitation: (1) Impacts of a sledge hammer: For each configuration, the structure was hit three times in each direction by the hammer at a location corresponding to Node 10 (Fig. 1); (2) Ambient vibration: The duration of the recorded data was 300 s for each configuration. (3) Electrodynamical shaker: The shaker was placed roughly at the center of one of the four bays on the roof, and a mass was attached to the end of the shaker to increase the excitation. The direction of the shaker force was perpendicular to a diagonal line of the roof. Two types of shaker force, random and sinusoidal sweep input, were used. Due to shaker–structure interaction, the shaker input force data were contaminated by the structural response, which is shown by its Fourier spectrum having resonant peaks at the natural frequencies of the benchmark structure. Based on the analysis results presented in Ching and Beck (2003a), the experimental mode shapes for the shaker cases have irregular appearances; consequently, reliable damage detection cannot be achieved, at least without the shaker–structure interaction being modeled. Such a study is left for future work.

Two sensor systems were mounted on the structure: Kinematics EPI sensor and FBA force–balance accelerometers. All sensors were clamped to the steel masses or structural members that they were mounted on. Five EPI sensors were mounted near the base and floor centers (Nodes 5, 14, 23, 32, and 41 in Fig. 1) to measure the accelerations in the  $+y$  direction, and ten FBA sensors were mounted near Nodes 2, 8, 11, 17, 20, 26, 29, 35, 38, and 44 in Fig. 1 to measure the accelerations in the  $+x$  direction. For

the loosened beam tests (Configs. 7–9), some of the sensors were moved to nearby locations so that they were not resting on a loose beam.

Results using a two-step probabilistic SHM approach (Beck et al. 2001; Vanik et al. 2000) are presented: the modal parameters and their uncertainties are identified in the first step and are then used in the subsequent step to determine the probability that stiffness reductions exceed a prescribed damage threshold. This approach was also used to analyze simulated Phase I (Yuen et al. 2004) but in this work a more reliable Bayesian updating algorithm [expectation–maximization (EM) algorithm] is proposed to find the most probable values of the model parameters.

## Model Updating Methodology

The primary purpose of the model updating methodology is to update the probability density function (PDF) of stiffness parameters of the identification model based on measured data from the undamaged and potentially damaged structure. The detection of damage is based on the probability that each substructure stiffness parameter has a fractional decrease of more than  $d$  from the undamaged to the potentially damaged structure, where the damage severity  $d$  is specified. The methodology consists of two steps where the first step involves identification of modal parameters and the associated uncertainties based on measured time–domain data, and the second step utilizes the outcome from the first step to compute the updated PDF of the stiffness parameters.

### Modal Parameter Identification

In the first step of the damage detection procedure, “experimental modal parameters” are extracted from the time domain measured acceleration data using the modal identification procedure called MODE-ID (Beck 1978, 1996; Beck et al. 1994). It is a nonlinear least-squares method based on a linear dynamical model with classical normal modes of vibration.

In the case of known excitation forces, MODE-ID estimates modal parameters of the structure by minimizing the Euclidean norm of the difference between the measured response of the structure and the model output at the measured degrees of freedom (DOF). The identified modal parameters are modal frequencies, damping ratios, participation factors, and mode shape components at the measured DOF for  $N_m$  dominant modes of vibration. The experimental modal parameters are then used for damage detection in the second step.

In the case of ambient-vibration input, extracting modal parameters is a challenging task because of the poor signal-to-noise ratio and the fact that the excitation forces are not known. In the approach used here (Beck et al. 1994), the excitation and structural responses are modeled as weakly stationary stochastic processes where the current excitation is assumed to be uncorrelated from the past response. It can be shown that the cross-correlation function matrix  $R_x(\tau)$  of the model responses satisfies the original equation of motion for the structure in free vibration where the time lag serves as a pseudotime

$$M\ddot{R}_x(\tau) + C\dot{R}_x(\tau) + KR_x(\tau) = 0 \quad (1)$$

where

$$R_x(\tau) = E[x(t)x^T(t-\tau)] \quad (2)$$

Here the derivatives are with respect to the time lag  $\tau$ . Each column vector of the cross-correlation function matrix  $R_x(\tau)$  is a free-vibration solution of the structure. Thus, modal identification is carried out by using the sample cross-correlation functions as free-vibration responses for MODE-ID. The identified modal parameters are the modal frequencies, damping ratios, and mode shape components at the measured DOF for  $N_m$  dominant modes of vibration.

The measured time histories of the structural response are partitioned temporally into  $N_s$  time segments, which are analyzed individually by the modal identification procedure to yield  $N_s$  sets of the modal parameters for the  $N_m$  modes. The experimental modal parameters are then used for damage detection in the second step.

### Damage Detection and Assessment

A general Bayesian statistical approach is employed to construct an updated PDF for the mass and stiffness parameters using a prior PDF and the experimental modal parameters from the first step (Beck and Katafygiotis 1998; Vanik et al. 2000). The prior PDF for the mass and stiffness parameters is specified to reflect the relative plausibilities of their values in the absence of any measurement data (Cox 1961).

To define the identification model class  $\mathcal{M}$ , we first choose a set of linear structural models with mass matrix  $M$  and stiffness matrix  $K$  parameterized in an affine manner as follows:

$$M(\rho) = M_0 + \sum_{i=1}^{N_M} \rho_i M_i \quad (3)$$

$$K(\theta) = K_0 + \sum_{i=1}^{N_K} \theta_i K_i$$

where  $M_i \in R^{N_d \times N_d}$  and  $K_i \in R^{N_d \times N_d}$  ( $N_d$ =number of DOF of the identification model) are prescribed nominal contributions of the  $i$ th substructure to the global mass and stiffness matrices, and the uncertain parameters  $\rho_i$  and  $\theta_i$  scale these contributions. We assume classical normal modes and thus the damping matrix  $C$  is not explicitly used.

In the situation that the full DOF of the identification model are not measured, "system mode shapes" (Vanik 1997; Vanik et al. 2000) may be introduced and the connection between the experimental modal parameters from the first step and the model parameters becomes

$$\hat{\omega}_{r,j}^2 = \tilde{\omega}_r^2 + \varepsilon_{r,j}, \quad \hat{\psi}_{r,j} = a_r \Gamma \phi_r + e_{r,j} \quad (4)$$

where  $\hat{\omega}_{r,j}$  and  $\hat{\psi}_{r,j} \in R^{N_o}$ =experimental modal frequency and mode shapes of the  $r$ th mode from the  $j$ th data segment ( $r=1 \dots N_m, j=1 \dots N_s$ );  $N_o$ =number of measured DOF,  $\phi_r \in R^{N_d}$ =system mode shape of the  $r$ th mode;  $\Gamma$ =matrix that picks the measured DOF from the system mode shape  $\phi_r$  (in the case where all DOF corresponding to the identification model are observed,  $\Gamma$  in Eq. (4) =identity matrix);  $a_r$ =scaling parameter (Vanik 1997; Vanik et al. 2000), and  $\tilde{\omega}_r$ =frequency given by the Rayleigh quotient

$$\tilde{\omega}_r^2 = \phi_r^T K(\theta) \phi_r / \phi_r^T M(\rho) \phi_r \quad (5)$$

which employs the system mode shape  $\phi_r$ , not the model mode shape corresponding to  $K(\theta)$  and  $M(\rho)$ . The experimental mode

shapes are normalized so that their Euclidean norm  $\|\hat{\psi}_{r,j}\|^2=1$ . We denote the set of experimental modal frequencies by  $\hat{\omega}=\{\hat{\omega}_{r,j}:r=1 \dots N_m, j=1 \dots N_s\}$ , the set of experimental mode shape components at the measured DOF by  $\hat{\psi}=\{\hat{\psi}_{r,j}:r=1 \dots N_m, j=1 \dots N_s\}$  and the set of system mode shapes by  $\phi=\{\phi_r:r=1 \dots N_m\}$  to facilitate future discussion. For conciseness, the symbol  $\mathcal{M}$  will be omitted in all derivations although all the PDFs are obviously conditional on the choice of  $\mathcal{M}$ .

The system mode shapes  $\phi$  can be regarded as a bridge connecting the identification problem with full mode shape information to the one with partial mode shape information. There are, however, several other advantages to expanding the identification model class  $\mathcal{M}$  by introducing the system mode shapes:

1. Because of the constraints of the assumed mathematical structure built into  $\mathcal{M}$ , it might not be possible for any structural model in this class to produce theoretical mode shapes that will give a good match of the experimental mode shapes. The system mode shapes provide extra flexibility in this aspect.
2. Their introduction also turns out to remove any need to match system and model modes during the identification, thereby avoiding a common difficulty in applications.
3. Finally, we will show that it is computationally beneficial to expand the model class  $\mathcal{M}$  by using the system mode shapes.

The two uncertainty terms in Eq. (4) are modeled as independent Gaussian variables, which is justified by the maximum differential entropy principle (Jaynes 1957; Rosenkrantz 1982)

$$\varepsilon_{r,j} \sim N(0, \sigma_r^2), \quad e_{r,j} \sim N(0, \delta_r^2 \cdot I) \quad (6)$$

The prior PDF of  $\rho$ ,  $\theta$ , and  $\phi$  is also chosen to be independent Gaussian with

$$\rho \sim N(\rho^0, P_\rho^0), \quad \theta \sim N(\theta^0, P_\theta^0) \quad (7)$$

subject to affine constraints  $A_\rho \rho + A_\theta \theta \leq b$ , and the variances of the prior PDFs of  $\phi_r$ ,  $\sigma_r^2$ ,  $\delta_r^2$ , and  $a_r$  are taken to be so large that the PDFs are essentially flat over the range of interest. It was reported in Yuen et al. (2004) that explicitly treating the uncertainties in the mass parameters  $\rho$  makes the identification more robust. However, to avoid making the identification problem ill-posed when simultaneously treating  $\rho$  and  $\theta$  as uncertain variables, we assume the variances of the prior PDF of  $\rho$  to be small.

### Most Probable Values of Model Parameters

The full set of model parameters is  $\lambda = \{\rho, \theta, \phi_r, a_r, \sigma_r^2, \delta_r^2: r=1 \dots N_m\}$ . The updated PDF of  $\lambda$  based on the experimental modal parameters from the first step, i.e.,  $p(\lambda | \hat{\omega}, \hat{\psi})$ , is of central concern in the Bayesian framework; in particular, the most probable values (MPVs) of the parameters based on the modal data are given by maximizing  $p(\lambda | \hat{\omega}, \hat{\psi})$ . For this optimization problem, it is more convenient to work with the logarithm of  $p(\lambda | \hat{\omega}, \hat{\psi})$

$$\begin{aligned} \log p(\lambda|\hat{\omega}, \hat{\psi}) = & -(1/2) \sum_{r=1}^{N_m} \sum_{j=1}^{N_s} [\{\log(\sigma_r^2) + (\hat{\omega}_{r,j}^2 - \tilde{\omega}_{r,j}^2)^2/\sigma_r^2\} + \{N_o \log(\delta_r^2) + \|\hat{\psi}_{r,j} - a_r \Gamma \phi_r\|^2/\delta_r^2\}] - (1/2) \{\log[\det(P_\rho^0)] \\ & + (\rho - \rho^0)^T (P_\rho^0)^{-1} (\rho - \rho^0)\} - (1/2) \{\log[\det(P_\theta^0)] + (\theta - \theta^0)^T (P_\theta^0)^{-1} (\theta - \theta^0)\} + c \end{aligned} \quad (8)$$

where  $c$ =constant. With the normalization condition  $\phi_r^T M \phi_r = 1$  and a fourth-order approximation error in the first term of  $p(\lambda|\hat{\omega}, \hat{\psi})$ , we show in the appendix I that  $p(\lambda|\hat{\omega}, \hat{\psi})$  can be rewritten as

$$\begin{aligned} \log p(\lambda|\hat{\omega}, \hat{\psi}) = & -(1/2) \sum_{r=1}^{N_m} \sum_{j=1}^{N_s} [\{\log(\sigma_r^2) + \|[K - \hat{\omega}_{r,j}^2 M] \phi_r\|_{M^{-1}}^2/\sigma_r^2\} + \{N_o \log(\delta_r^2) + \|\hat{\psi}_{r,j} - a_r \Gamma \phi_r\|^2/\delta_r^2\}] - (1/2) \{\log[\det(P_\rho^0)] \\ & + (\rho - \rho^0)^T (P_\rho^0)^{-1} (\rho - \rho^0)\} - (1/2) \{\log[\det(P_\theta^0)] + (\theta - \theta^0)^T (P_\theta^0)^{-1} (\theta - \theta^0)\} + c \end{aligned} \quad (9)$$

The advantage of converting Eq. (8) to (9) is that  $\log p(\lambda|\hat{\omega}, \hat{\psi})$  is not quadratic in  $\phi$  in Eq. (8), but it is quadratic in  $\phi$  in Eq. (9). Being quadratic in  $\phi$  has certain computational benefits, as shown later.

If the identification model is globally identifiable (Beck and Katafygiotis 1998), the updated PDF  $p(\lambda|\hat{\omega}, \hat{\psi})$  can be asymptotically approximated by a multidimensional Gaussian PDF with mean that is equal to the MPV of  $\lambda$ , where

$$\hat{\lambda} = \arg \max_{\lambda} \log p(\lambda|\hat{\omega}, \hat{\psi}) \quad (10)$$

subject to affine constraints  $A_p \rho + A_\theta \theta \leq b$ , and the covariance matrix that is equal to the negative of the inverse of the Hessian matrix  $H(\hat{\lambda}|\hat{\omega}, \hat{\psi})$ , where

$$H(\lambda|\hat{\omega}, \hat{\psi}) = \nabla_{\lambda} \nabla_{\lambda} \log p(\lambda|\hat{\omega}, \hat{\psi}) \quad (11)$$

The optimization problem associated with Eq. (10) may have more than one local maximum since  $\log p(\lambda|\hat{\omega}, \hat{\psi})$  is not a concave function of  $\lambda$ . Also,  $\log p(\lambda|\hat{\omega}, \hat{\psi})$  does not fall into certain functional forms that are easy to optimize, e.g., linear or quadratic functions. Such a problem is usually handled using a local search optimization algorithm based on Newton's methods or ascent methods. However, due to the high dimensionality of  $\lambda$ , the use of such local search methods, which often require evaluation of gradients or Hessians with respect to  $\lambda$ , is computationally challenging.

Notice that given  $\{\rho, \theta, a_r, \sigma_r^2, \delta_r^2: r=1 \dots N_m\}$ ,  $\log p(\lambda|\hat{\omega}, \hat{\psi})$  in Eq. (9) is concave in  $\phi$ . Also, given  $\phi$  and  $\rho$  (and so the mass matrix  $M$ ), and that the system is locally identifiable based on the modal data (Beck and Katafygiotis 1998), finding the MPV of  $\{\theta, a_r, \sigma_r^2, \delta_r^2: r=1 \dots N_m\}$  is equivalent to estimating the mean and covariance matrix of a Gaussian PDF based on sampled data, which is a well-known concave optimization problem with a unique local maximum. Moreover, given  $\phi$ ,  $\log p(\lambda|\hat{\omega}, \hat{\psi})$  is quadratic in  $\theta$  and roughly quadratic in  $\rho$  (this is because the prior PDF of  $\rho$  has small variances). This suggests a strategy to maximize the objective function  $\log p(\lambda|\hat{\omega}, \hat{\psi})$  alternatively with respect to  $\phi$  and  $\{\rho, \theta, a_r, \sigma_r^2, \delta_r^2: r=1 \dots N_m\}$  until satisfactory convergence is achieved. In this way, we decompose the nonconcave optimization problem into two coupled concave and quadratic optimization problems. This strategy solves the optimization difficulty mentioned above since the solutions of the two quadratic programming problems can be computed analytically and rapidly. Moreover, this strategy is, in fact, closely related to the EM algorithm (Shumway and Stoffer 1982).

The EM algorithm deals with the problem of probabilistic inference and parameter estimation when some uncertain variables are not observed. In our case, the unobserved variable is the system mode shape  $\phi$ , while the parameters we intend to estimate are  $\{\theta, a_r, \sigma_r^2, \delta_r^2: r=1 \dots N_m\}$  based on the observed  $\hat{\omega}$  and  $\hat{\psi}$ . In the appendix II, a special EM algorithm, called the tight EM (TEM) algorithm is presented. The TEM algorithm is an ascent algorithm for  $\log p(\lambda|\hat{\omega}, \hat{\psi})$ , i.e.,  $\log p(\lambda^{(i)}|\hat{\omega}, \hat{\psi})$  always increases during the TEM iterations and so  $\lambda^{(i)}$  approaches the MPV of  $\lambda$ . The TEM algorithm is used in this study to find the MPV of the stiffness parameters based on the experimental Phase II benchmark data.

The EM algorithm solves the optimization difficulty mentioned in the beginning of this section since it decomposes the high-dimensional nonconcave optimization problem into two coupled concave optimization problems with analytical solutions. In our experience, when a nonlinear programming algorithm, e.g., a quasi-Newton or steepest ascent algorithm, is used to find the MPV, the solution sometimes can be trapped in a local minimum away from the MPV even when the initial search point is close to the MPV. We find that the EM algorithm is robust in the sense that the initial point does not have to be close to the MPV in order to converge to the MPV. Nevertheless, the convergence of the EM algorithm sometimes can be quite slow.

### Probability of Damage

The marginal updated PDF of  $\theta_i$ ,  $p(\theta_i|\hat{\omega}, \hat{\psi})$ , obtained by integrating the joint updated PDF to remove the other parameters in  $\lambda$ , can be used to find the probability that the  $i$ th substructure stiffness parameter has been reduced by more than a specified fraction  $d_i$  of the stiffness in the initial undamaged state of the structure. By using the Gaussian asymptotic approximation (see Papadimitriou et al. 1997; Beck and Katafygiotis 1998) and assuming the stiffness parameters for the undamaged state and possibly damage state are conditionally independent (Beck et al. 2001), we get

$$\begin{aligned} P_i(d_i) = & P\{\theta_i^{\text{pd}} < (1 - d_i)\theta_i^{\text{ud}} | \hat{\omega}^{\text{pd}}, \hat{\psi}^{\text{pd}}, \hat{\omega}^{\text{ud}}, \hat{\psi}^{\text{ud}}\} \\ \approx & \Phi \left( \frac{(1 - d_i)\hat{\theta}_i^{\text{ud}} - \hat{\theta}_i^{\text{pd}}}{\sqrt{(1 - d_i^2)(\hat{\sigma}_i^{\text{ud}})^2 + (\hat{\sigma}_i^{\text{pd}})^2}} \right) \end{aligned} \quad (12)$$

where  $\Phi(\cdot)$ =standard Gaussian cumulative distribution function,  $\hat{\theta}_i^{\text{ud}}$  and  $\hat{\theta}_i^{\text{pd}}$  denote the MPV of the stiffness parameters for an undamaged and possibly damaged structure, respectively; and  $\hat{\sigma}_i^{\text{ud}}$  and  $\hat{\sigma}_i^{\text{pd}}$ =corresponding standard deviations from the covariance matrix derived from the Hessian matrix in Eq. (11).

**Table 1.** Experimental Modal Parameters for Hammer Cases

	Frequency (Hz)								Damping ratio (%)							
	W1 <sup>a</sup>	S1 <sup>a</sup>	T1 <sup>a</sup>	W2	S2	T2	W3	S3	W1 <sup>a</sup>	S1 <sup>a</sup>	T1 <sup>a</sup>	W2	S2	T2	W3	S3
Config1.h	7.45	7.67	14.45	19.84	20.87	—	—	—	0.73	0.78	0.46	0.32	0.42	—	—	—
COV <sup>b</sup> (%)	0.02	0.05	0.01	0.01	0.04	—	—	—	7.80	0.87	5.42	7.38	1.44	—	—	—
Config2.h	7.68	5.12	12.69	19.99	14.92	—	—	—	0.66	0.88	0.38	0.37	0.48	—	—	—
COV <sup>b</sup> (%)	0.04	0.06	0.02	0.02	0.03	—	—	—	2.47	2.29	1.78	2.14	0.15	—	—	—
Config3.h	7.56	6.52	13.40	19.91	18.78	—	—	—	0.69	0.79	0.34	0.39	0.46	—	—	—
COV <sup>b</sup> (%)	0.01	0.08	0.00	0.02	0.07	—	—	—	1.57	2.09	1.11	1.96	5.19	—	—	—
Config4.h	7.56	7.26	13.95	20.05	19.67	—	—	—	0.70	0.65	0.37	0.56	0.32	—	—	—
COV <sup>b</sup> (%)	0.02	0.03	0.01	0.10	0.01	—	—	—	0.53	0.72	4.26	25.74	0.51	—	—	—
Config5.h	7.55	7.37	13.99	19.84	20.48	—	—	—	0.64	0.65	0.33	0.31	0.39	—	—	—
COV <sup>b</sup> (%)	0.07	0.01	0.02	0.05	0.01	—	—	—	5.33	1.48	1.75	6.71	4.27	—	—	—
Config6.h	5.93	7.68	13.07	19.81	20.80	—	—	—	0.60	0.82	0.43	0.32	0.47	—	—	—
COV <sup>b</sup> (%)	0.05	0.04	0.02	0.02	0.04	—	—	—	5.14	1.11	1.81	4.44	3.17	—	—	—
Config7.h	2.62	3.60	4.31	8.44	11.94	13.88	16.16	21.58	0.92	0.94	0.77	0.44	0.51	0.51	0.30	0.38
COV <sup>b</sup> (%)	0.08	0.05	0.02	0.02	0.04	0.01	0.01	0.03	6.69	2.78	1.96	0.83	0.18	1.95	3.42	2.03
Config8.h	2.54	3.24	4.10	8.28	11.03	13.28	15.92	20.61	0.90	1.06	0.80	0.45	0.59	0.46	0.31	0.59
COV <sup>b</sup> (%)	0.01	0.06	0.03	0.03	0.16	0.04	0.03	0.06	3.91	1.01	2.01	1.81	2.56	0.68	1.59	1.75
Config9.h	2.56	3.35	4.15	8.38	11.67	13.60	16.05	21.08	0.96	1.09	0.86	0.45	0.55	0.53	0.32	0.65
COV <sup>b</sup> (%)	0.06	0.14	0.04	0.01	0.03	0.02	0.01	0.04	3.13	5.15	1.29	0.31	1.85	0.62	0.30	0.69

<sup>a</sup>W1, S1, and T1 mean the corresponding values for the first mode in the weak, strong directions, and torsion, respectively.

<sup>b</sup>Coefficient of variation.

## Results for Experimental Phase II Benchmark

For each configuration (Configs. 1–9) and each type of excitation (hammer or ambient vibrations), the experimental time histories are divided into three segments to yield three sets of independent estimates ( $N_s=3$ ) of the experimental modal parameters. All acceleration data are filtered by a Butterworth high-pass filter with cutoff frequency equal to 0.1 Hz to eliminate the mean and drift. We will label a configuration using its configuration number augmented by the excitation type ( $h$  and  $a$  stand for hammer and ambient vibrations, respectively), e.g., Config2.h denotes Configuration 2 with the hammer excitation.

## Modal Identification

For the braced cases (Configs. 1–6), five modes ( $N_m=5$ ), including the first and second translation modes in the  $x$  and  $y$  directions and the first torsion mode, are identified using MODE-ID. For the unbraced cases (Configs. 7–9), only the hammer excitation is studied, and eight modes ( $N_m=8$ ), including the first, second, and third translation modes in the  $x$  and  $y$  directions and the first and second torsion modes, are identified. Tables 1 and 2 show the average values of the experimental modal frequencies for all excitation types. The corresponding values of the coefficient of variation (COV), defined as the ratio of the standard error to the

**Table 2.** Experimental Modal Parameters for Ambient-Vibration Cases

	Frequency (Hz)				
	W1	S1	T1	W2	S2
Config1.a	7.48	7.76	14.48	19.89	21.01
COV <sup>a</sup> (%)	0.29	0.16	0.04	0.00	0.01
Config2.a	7.73	5.19	12.74	20.12	15.02
COV <sup>a</sup> (%)	0.11	0.17	0.13	0.25	0.04
Config3.a	7.63	6.65	13.44	20.03	18.87
COV <sup>a</sup> (%)	0.28	0.03	0.03	0.03	0.02
Config4.a	7.60	7.36	13.98	20.11	19.68
COV <sup>a</sup> (%)	0.16	0.26	0.07	0.04	0.14
Config5.a	7.61	7.46	14.02	19.89	20.00
COV <sup>a</sup> (%)	0.27	0.25	0.15	0.02	0.18
Config6.a	5.97	7.77	13.20	19.89	21.00
COV <sup>a</sup> (%)	0.15	0.53	0.28	0.01	0.00

<sup>a</sup>Coefficient of variation.

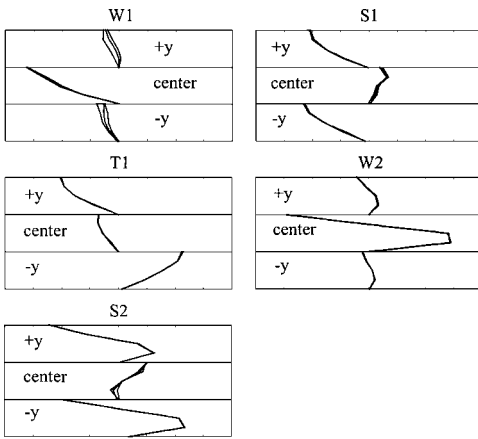


Fig. 2. Experimental mode shape components for Config1.h

mean value, are shown in percent in these tables. The variability for the ambient–vibration excitation is significantly larger than that for the hammer excitation. This is due to the fact that the input excitation is unknown, while it is known that the input excitation for the hammer is zero after the impulsive force.

The experimental damping ratios for the hammer excitation are also shown in Table 1. Significantly larger values of COV are observed for damping ratios than modal frequencies in most cases, although some damping ratios show small COV, probably due to the fact that the COV values are based on only  $N_s=3$  samples. This suggests that, as far as the current study is concerned, although the modal frequencies and mode shapes can be identified reasonably well, more information, especially about the excitation, is needed to identify the damping ratios more precisely. The experimental damping ratios for the ambient vibration excitation, which are not presented here, all show a large COV, indicating that the estimates are not reliable. However, the damage detection and assessment method that we employ does not use damping estimates.

The fifteen acceleration measurements, ten on the +y and -y faces of the structure sensing the x (strong) direction and five at the floor centers sensing the y (weak) direction, are used to identify the modeshape components at the +y -y faces and the center of the structure, which are plotted in Figs. 2 and 3 for Config1.h and Config.1.a (for other configurations, the experimental mode shapes are similar and the corresponding plots can be found in Ching and Beck 2003a). The mode shapes identified for each of

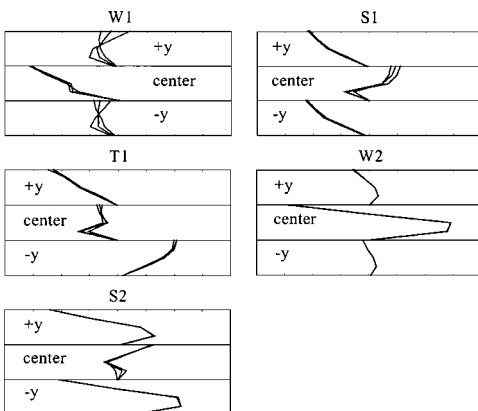


Fig. 3. Experimental mode shape components for Config1.a

the  $N_s=3$  time segments are plotted in each figure. Notice that for the ambient–vibration cases (e.g., Fig. 3), there are unusual kinks in many of the mode shape components measured at the floor centers. The experimental mode shapes for the hammer excitation have smaller variability than those for the ambient–vibration excitation.

## Damage Detection and Assessment

### Braced Cases (Configs. 1–6)

A three dimensional (3D) 12 DOF shear building model is used for damage detection for the braced cases. The model assumes rigid floors, and three DOF, translations along the x and y axes and rotation about the z axis, are assigned to each floor to give 12 DOF. In order to locate the faces sustaining damage, four stiffness parameters are used for each story to give 16 stiffness parameters

$$K(\theta) = \sum_i \sum_j \theta_{ij} \bar{K}_{ij} \quad (13)$$

where  $i=1, \dots, 4$ ,  $j=+x, -x, +y, -y$ , and the indices  $i$  and  $j$  denote the story number and the direction of the outward normal of a face, respectively. The  $\bar{K}_{ij}$  are the “nominal” stiffness matrices computed based on shear building assumptions for the original undamaged structure. The stiffness model was originally proposed in Yuen et al. (2004) and yielded satisfactory damage detection results for the Phase I (Yuen et al. 2004) and Phase II (Ching and Beck 2003a, b) simulated benchmark studies. The prior PDF on the 16 stiffness parameters is taken to be independent Gaussian with mean and COV equal to 1 and 20% with the following affine constraints to reflect the fact that the stiffness parameters for damaged cases can only be less than those of the reference case:

$$0 \leq \theta_i \leq (1 + 2\hat{\zeta}_i^{\text{Config1}})\hat{\theta}_i^{\text{Config1}} \quad (14)$$

where  $\hat{\theta}_i^{\text{Config1}} = \text{MPV}$  of  $\theta_i$  from Config. 1, and  $\hat{\zeta}_i^{\text{Config1}} = \text{corresponding COV}$ . The prior COV is chosen to be 20% since if we know a priori that the damage is in braces only, the largest possible reduction in the stiffness parameter is roughly 40% (computed based on shear building assumptions), which is twice the chosen prior standard deviation. Therefore, the probability that the updated stiffness is less than 60% of the nominal stiffness is relatively small.

In calculating the nominal story masses, the mass of the columns is lumped at the floors that they are connected to. One mass parameter is used for each story to give four mass parameters

$$M(\rho) = \sum_i \rho_i \bar{M}_i \quad (15)$$

where  $i=1, \dots, 4$  represents the story number and the  $\bar{M}_i$  = nominal mass matrices computed based on the original undamaged structure. Each  $\bar{M}_i$  is computed based on the mass distribution of the test structure, i.e., the floor mass is 1,000, 1,000, 1,000, and 750 kg for the first, second, third, and fourth floors. The prior PDF for the uncertain mass parameters is taken to be independent Gaussian with mean and COV equal to 1 and 0.1%. This means that the mass is effectively held at its most probable (nominal) value.

Based on the results from the TEM algorithm, the ratios of the MPV of the stiffness parameters for Configs. 2–6 with respect to those for the undamaged (Config. 1) case are tabulated in Tables 3 and 4 for the two excitation types. The corresponding COV is

**Table 3.** Stiffness Ratios for Braced Hammer Cases

	$\theta_{1,+x}$	$\theta_{2,+x}$	$\theta_{3,+x}$	$\theta_{4,+x}$	$\theta_{1,+y}$	$\theta_{2,+y}$	$\theta_{3,+y}$	$\theta_{4,+y}$	$\theta_{1,-x}$	$\theta_{2,-x}$	$\theta_{3,-x}$	$\theta_{4,-x}$	$\theta_{1,-y}$	$\theta_{2,-y}$	$\theta_{3,-y}$	$\theta_{4,-y}$
Config1.h	1.00	1.00	1.00	1.00	1.00	1.00	1.00	1.00	1.00	1.00	1.00	1.00	1.00	1.00	1.00	1.00
COV <sup>a</sup> (%)	2.86	8.02	2.37	2.74	9.61	9.36	6.87	8.76	2.79	7.71	2.52	2.95	8.45	10.25	7.93	10.54
Config2.h	1.03	0.88	0.96	1.03	1.19	0.95	1.03	1.01	1.06	0.90	0.96	0.98	<b>0.16*</b>	<b>0.26*</b>	<b>0.25*</b>	<b>0.12*</b>
COV <sup>a</sup> (%)	1.94	4.78	1.50	1.82	9.36	9.63	9.32	10.63	1.91	4.86	1.60	1.88	43.75	29.71	24.32	47.59
Config3.h	1.06	0.94	0.95	0.94	1.19	0.95	1.14	1.03	1.06	1.07	0.95	0.92	<b>0.55*</b>	<b>0.71*</b>	<b>0.49*</b>	<b>0.53*</b>
COV <sup>a</sup> (%)	2.50	8.01	1.87	2.02	6.02	8.23	4.24	4.93	2.38	7.18	1.98	2.14	6.84	12.69	5.98	6.65
Config4.h	1.06	1.12	1.01	1.01	1.19	0.90	1.03	1.08	1.05	1.08	1.01	0.94	<b>0.57*</b>	1.20	0.98	<b>0.61*</b>
COV <sup>a</sup> (%)	2.51	9.44	1.93	2.17	8.66	9.47	6.54	6.92	2.29	8.29	2.00	2.24	10.37	9.34	6.72	8.55
Config5.h	1.01	0.92	0.96	1.01	1.19	0.93	1.00	1.01	1.02	1.02	0.96	0.98	<b>0.59*</b>	0.96	0.97	0.97
COV <sup>a</sup> (%)	3.66	9.52	3.09	3.59	8.06	8.82	6.71	8.48	3.57	7.92	3.32	3.97	10.96	9.52	7.06	9.54
Config6.h	1.06	<b>0.63*</b>	0.95	0.99	0.97	0.85	0.94	0.92	1.06	1.15	0.92	0.93	1.03	0.89	0.96	0.99
COV <sup>a</sup> (%)	2.42	11.94	1.83	2.05	11.26	11.78	8.48	10.43	2.36	8.35	2.08	2.31	10.56	11.96	10.30	14.01

<sup>a</sup>Coefficient of variation.

also shown [calculated using the Hessian matrix of  $\log p(\lambda | \hat{\omega}, \hat{\psi})$  as described earlier]. The stiffness parameters whose reductions are significantly greater than their COV are marked with asterisks. The actual damaged locations are made bold faced for comparison.

For the hammer excitation, all brace damage is detected, and no false detection is found. Using shear building assumptions, the theoretical stiffness ratios for a particular face with removal of one and two braces are 77.4 and 54.87%, respectively. However, the identified stiffness ratios for faces with removal of one and two braces are around 60 and 20%, respectively. Despite this inconsistency, the estimates for the stiffness losses are internally consistent, i.e., removal of one and two braces corresponds to 40 and 80% reduction in stiffness, respectively. The probabilities of damage,  $P_{ij}(d)$ , for the hammer cases are plotted in Fig. 4 for Config2.h (the plots for other braced cases can be found in Ching and Beck 2003a).

For the ambient–vibration excitation, all damage is also detected. The identified stiffness ratios are close to those for the hammer cases. Seven false detections are found, however, and the four false detections in  $\theta_{2,-x}$  indicate significant stiffness reduction (18–44%). These are probably due to the unusual kinks exhibited in the experimental mode shape components measured at the floor centers. For other false detections, the identified stiffness reductions are moderate (all less than 26%). The plots of the probabilities of damage,  $P_{ij}(d)$ , for the ambient–vibration cases can be found in Ching and Beck (2003a).

**Unbraced Cases (Configs. 7–9)**

For the unbraced cases, a 3D 36 DOF model that assumes rigid floors in the  $x$ – $y$  plane and allows rotation about the  $x$  and  $y$  axes is proposed. All nodes at the same story are assumed to have identical  $x$  and  $y$  direction translations, and the floor is assumed to be rigid with respect to rotation about the  $z$  axis to give 3 of the 9 DOF, for each story. Nodes are allowed to rotate about the  $x$  and  $y$  axes in a constrained way: nodes in each floor with the same  $x$  coordinates or same  $y$  coordinates are assumed to have the same amount of rotation about the  $y$  and  $x$  axes, respectively, to give the remaining 6 DOF for each floor (that is, rotation about each of the three frame lines in each direction). Translation along the  $z$  direction is not allowed in this model. It is noted that there are 36 DOF in the model and only 12 DOF are measured, but this poses no problems for the TEM algorithm in finding the MPV of the model parameters.

Two parameters are used for the rotational stiffness in each floor: it is assumed that the rotational stiffness of all beam–column connections in the same floor about the  $x$  axis (or about the  $y$  axis) is identical. Besides the rotational stiffness, two parameters are used for the strong ( $x$ ) direction and weak ( $y$ ) direction column stiffness to give ten stiffness parameters in total

$$K(\theta) = \theta_{c,x} \bar{K}_{c,x} + \theta_{c,y} \bar{K}_{c,y} + \sum_i \sum_j \theta_{ij} \bar{K}_{ij} \quad (16)$$

where  $i=1, \dots, 4$ ,  $j=x$  and  $y$ , and the indices  $i$  and  $j$  denote the story number and the axis about which the rotational stiffness is

**Table 4.** Stiffness Ratios for Braced Ambient–Vibration Cases

	$\theta_{1,+x}$	$\theta_{2,+x}$	$\theta_{3,+x}$	$\theta_{4,+x}$	$\theta_{1,+y}$	$\theta_{2,+y}$	$\theta_{3,+y}$	$\theta_{4,+y}$	$\theta_{1,-x}$	$\theta_{2,-x}$	$\theta_{3,-x}$	$\theta_{4,-x}$	$\theta_{1,-y}$	$\theta_{2,-y}$	$\theta_{3,-y}$	$\theta_{4,-y}$
Config1.a	1.00	1.00	1.00	1.00	1.00	1.00	1.00	1.00	1.00	1.00	1.00	1.00	1.00	1.00	1.00	1.00
COV <sup>a</sup> (%)	2.56	5.21	2.13	2.39	13.99	13.83	7.08	8.89	2.59	5.14	2.24	2.55	11.17	18.40	8.73	10.12
Config2.a	1.05	0.89	0.98	0.98	1.28	1.06	1.14	1.18	1.05	0.82*	0.97	0.94	<b>0.30*</b>	<b>0.52*</b>	<b>0.35*</b>	<b>0.19*</b>
COV <sup>a</sup> (%)	2.63	5.08	2.04	2.40	12.17	10.66	10.86	13.97	2.69	5.16	2.12	2.43	34.84	20.49	22.71	34.20
Config3.a	1.05	0.83*	0.95	0.94	1.28	1.13	1.14	1.18	1.05	0.56*	0.97	0.94	<b>0.65*</b>	<b>0.50*</b>	<b>0.47*</b>	<b>0.51*</b>
COV <sup>a</sup> (%)	3.11	7.25	2.19	2.33	5.87	6.18	3.92	4.93	2.92	8.95	2.14	2.36	6.50	13.17	5.92	6.41
Config4.a	1.05	0.88	0.96	0.97	1.28	1.08	0.97	1.18	1.05	0.56*	0.97	0.90	<b>0.66*</b>	1.13	0.93	<b>0.56*</b>
COV <sup>a</sup> (%)	4.00	6.46	2.88	3.28	6.61	7.16	5.02	5.45	3.81	8.60	2.90	3.36	8.32	8.86	5.11	6.60
Config5.a	1.03	1.10	0.90	0.94	0.97	0.78	0.74*	0.76*	1.05	0.94	1.03	1.04	<b>0.55*</b>	0.78	1.17	1.13
COV <sup>a</sup> (%)	3.07	13.56	2.84	3.03	5.22	7.48	4.16	5.18	3.08	11.50	2.67	3.05	8.43	8.44	4.07	4.74
Config6.a	1.05	<b>0.76*</b>	0.96	0.96	1.06	0.81	0.89	0.84	1.05	0.69*	0.99	0.97	1.07	0.94	1.17	0.87
COV <sup>a</sup> (%)	2.38	7.89	1.89	2.08	6.61	6.32	6.34	8.74	2.42	9.84	2.05	2.23	6.89	6.59	6.87	10.23

<sup>a</sup>Coefficient of variation.

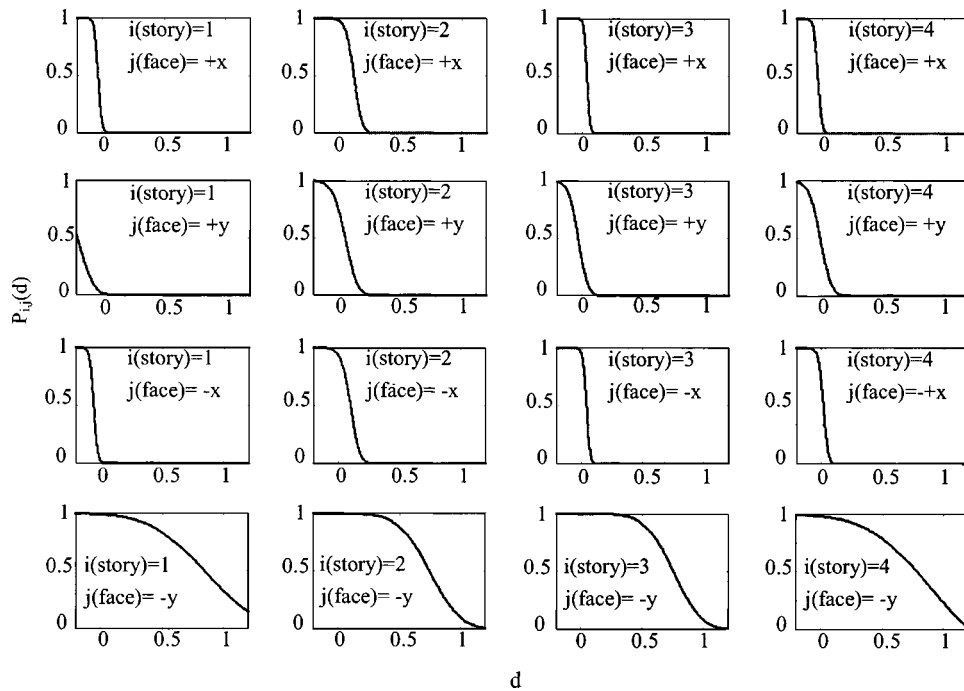


Fig. 4. Probability  $P_{ij}(d)$  of damage exceeding  $d$  in each substructure (config2.h).

active, respectively; the  $\bar{K}_{ij}$ =nominal rotational stiffness matrices computed based on the model assumptions for the original undamaged structure;  $\bar{K}_{c,x}$  and  $\bar{K}_{c,y}$ = $x$  and  $y$  directions, respectively, nominal stiffness matrices contributed by the columns. This stiffness model was originally proposed in Ching and Beck (2003a, c) where it yielded satisfactory damage detection results for beam-column connection failures for the Phase II simulated benchmark studies.

Due to the fact that the stiffness matrix of the unbraced benchmark structure is dominated by the stiffness of the columns, which also provide rotational stiffness, slight errors in the identified column stiffness parameters will significantly influence the values of the identified rotational stiffness parameters. This indicates that in order to reliably detect and assess rotational stiffness damage, sufficient prior information about the column stiffness is needed. Therefore, the prior PDF on the two column stiffness parameters is taken to be independent Gaussian with mean and COV equal to 1 and 1%, which expresses high confidence in the nominal column stiffness values that may not be fully justified. The prior PDF of the eight rotational stiffness parameters is taken to be independent Gaussian with mean and COV equal to 1 and 20%. The affine inequality constraints are identical to Eq. (14) except that  $\hat{\theta}_i^{\text{Config1}}$  and  $\hat{\zeta}_i^{\text{Config1}}$  are replaced by  $\hat{\theta}_i^{\text{Config7}}$  and  $\hat{\zeta}_i^{\text{Config7}}$ . The mass of the columns is lumped at the floors that they are

connected to, and one mass parameter is used for each story to give four mass parameters. The prior PDF for the uncertain mass parameters is taken to be independent Gaussian with mean and COV equal to 1 and 0.1%.

Only the hammer cases are considered for the unbraced cases since the corresponding experimental mode shapes have the best quality. In all the cases considered, the stiffness and mass parameters are found to be globally identifiable. The ratios between the MPV of the stiffness parameters for Config8.h and Config9.h with respect to those for Config7.h are tabulated in Table 5, with the corresponding COV shown. Although most damage except for  $\theta_{4,y}$  of Config8.h is detected, many false detections are found, and some of them indicate significant stiffness reduction. It is believed that the poor performance is due to the fact that the stiffness matrix of the structure is dominated by the columns, rendering the identification of rotational stiffness difficult. In the simulated Phase II benchmark, our methodology has successfully detected rotational stiffness damage II (Ching and Beck 2003c) probably because the modeling error was relatively small. For the experimental Phase II benchmark, the modeling error in the column stiffness may be too large to have the rotational stiffness damage reliably detected. Since the results of the damage detection are poor, the plots for the probability of damage, as well as the identified system mode shapes, are not shown.

Table 5. Stiffness Ratios for Unbraced Hammer Cases

	$\theta_{c,x}$	$\theta_{c,y}$	$\theta_{1,x}$	$\theta_{2,x}$	$\theta_{3,x}$	$\theta_{4,x}$	$\theta_{1,y}$	$\theta_{2,y}$	$\theta_{3,y}$	$\theta_{4,y}$
Config7.h	1.00	1.00	1.00	1.00	1.00	1.00	1.00	1.00	1.00	1.00
COV <sup>a</sup> (%)	0.11	0.09	0.40	0.50	0.37	0.79	0.41	0.37	0.33	0.46
Config8.h	0.99	0.97*	0.87*	1.01	0.78*	0.62*	<b>0.65*</b>	<b>0.52*</b>	<b>0.52*</b>	<b>0.97</b>
COV <sup>a</sup> (%)	0.06	0.19	0.09	0.10	0.15	0.40	13.44	2.99	7.77	1.85
Config9.h	0.97*	0.98*	0.94*	1.01	0.82*	0.86*	<b>0.84*</b>	<b>0.72*</b>	0.87*	0.99
COV <sup>a</sup> (%)	0.16	0.13	0.40	0.45	0.75	1.88	0.63	0.67	0.98	0.72

<sup>a</sup>Coefficient of variation.

## Conclusion

The two-step Bayesian probabilistic structural health monitoring approach is used to analyze the IASC–ASCE Phase II experimental benchmark data. For the braced cases, the damage can be detected reliably for the hammer and ambient–vibration excitations. For the unbraced cases, reliable damage detection cannot be achieved, probably due to the dominance of the column stiffness and large modeling errors. The proposed tight expectation–maximization algorithm for searching for the most probable val-

ues of the stiffness parameters is found to be robust compared to standard nonlinear programming algorithms.

## Appendix I. Approximation in Eq. (9)

In this appendix, we show that Eq. (8) can be converted to Eq. (9) using the normalization condition  $\phi_r^T M \phi_r = 1$  and a fourth-order approximation error for the first term in  $p(\lambda | \hat{\omega}, \hat{\psi})$ . For convenience, Eq. (8) is rewritten here

$$\log p(\lambda | \hat{\omega}, \hat{\psi}) = - (1/2) \sum_{r=1}^{N_m} \sum_{j=1}^{N_s} [\{\log(\sigma_r^2) + (\hat{\omega}_{r,j}^2 - \tilde{\omega}_r^2)^2 / \sigma_r^2\} + \{N_o \log(\delta_r^2) + \|\hat{\psi}_{r,j} - a_r \Gamma \phi_r\|^2 / \delta_r^2\}] - (1/2) \{\log[\det(P_\rho^0)] + (\rho - \rho^0)^T (P_\rho^0)^{-1} (\rho - \rho^0)\} - (1/2) \{\log[\det(P_\theta^0)] + (\theta - \theta^0)^T (P_\theta^0)^{-1} (\theta - \theta^0)\} + c \quad (17)$$

where  $c = \text{constant}$ . With the normalization condition  $\phi_r^T M \phi_r = 1$ , we have

$$\begin{aligned} (\hat{\omega}_{r,j}^2 - \tilde{\omega}_r^2)^2 &= (\hat{\omega}_{r,j}^2)^2 - 2\hat{\omega}_{r,j}^2 \tilde{\omega}_r^2 + (\tilde{\omega}_r^2)^2 = \frac{[\phi_r^T K M^{-1} K \phi_r + (\hat{\omega}_{r,j}^2)^2 \phi_r^T M \phi_r - 2 \cdot \hat{\omega}_{r,j}^2 \phi_r^T K \phi_r] - [\phi_r^T K M^{-1} K \phi_r + (\tilde{\omega}_r^2)^2 \phi_r^T M \phi_r - 2 \cdot \tilde{\omega}_r^2 \phi_r^T K \phi_r]}{\phi_r^T M \phi_r} \\ &= [(K - \hat{\omega}_{r,j}^2 M) \phi_r]^T M^{-1} [(K - \hat{\omega}_{r,j}^2 M) \phi_r] - [(K - \tilde{\omega}_r^2 M) \phi_r]^T M^{-1} [(K - \tilde{\omega}_r^2 M) \phi_r] = \|(K - \hat{\omega}_{r,j}^2 M) \phi_r\|_{M^{-1}}^2 - \|(K - \tilde{\omega}_r^2 M) \phi_r\|_{M^{-1}}^2 \quad (18) \end{aligned}$$

Among the terms in Eq. (18),  $\|(K - \tilde{\omega}_r^2 M) \phi_r\|_{M^{-1}}^2$  is significantly less than  $\|(K - \hat{\omega}_{r,j}^2 M) \phi_r\|_{M^{-1}}^2$  if  $\phi_r$  is close to a theoretical mode shape  $\phi_r^{\text{Th}}$  of the structural model. Indeed, if  $\phi_r$  is equal to  $\phi_r^{\text{Th}}$ ,  $\tilde{\omega}_r$  will simply be the theoretical modal frequency; therefore  $\|(K - \tilde{\omega}_r^2 M) \phi_r\|_{M^{-1}}^2$  vanishes. Furthermore, if  $\phi_r$  is close to  $\phi_r^{\text{Th}}$  with a small perturbation  $\delta \phi_r$ ,

$$\begin{aligned} \|(K - \tilde{\omega}_r^2 M) \phi_r\|_{M^{-1}} |_{\phi_r = \phi_r^{\text{Th}} + \delta \phi_r} &= \|(K - \tilde{\omega}_r^2 M) \phi_r\|_{M^{-1}} |_{\phi_r = \phi_r^{\text{Th}}} \\ &+ \nabla_{\phi_r} \|(K - \tilde{\omega}_r^2 M) \phi_r\|_{M^{-1}} |_{\phi_r = \phi_r^{\text{Th}}} \cdot \delta \phi_r \\ &+ 1/2 \cdot \delta \phi_r^T \cdot \nabla_{\phi_r}^2 \|(K - \tilde{\omega}_r^2 M) \phi_r\|_{M^{-1}} |_{\phi_r = \phi_r^{\text{Th}}} \cdot \delta \phi_r \\ &+ O(\|\delta \phi_r\|^3) \quad (19) \end{aligned}$$

Since we know that

$$\|(K - \tilde{\omega}_r^2 M) \phi_r\|_{M^{-1}} |_{\phi_r = \phi_r^{\text{Th}}} = 0 \quad (20)$$

and that

$$\nabla_{\phi_r} \|(K - \tilde{\omega}_r^2 M) \phi_r\|_{M^{-1}} |_{\phi_r = \phi_r^{\text{Th}}} \cdot \delta \phi_r = 0 \quad (21)$$

i.e.,  $\|(K - \tilde{\omega}_r^2 M) \phi_r\|_{M^{-1}}$  is stationary with respect to  $\phi_r$  at  $\phi_r^{\text{Th}}$ , we conclude that  $\|(K - \tilde{\omega}_r^2 M) \phi_r\|_{M^{-1}}^2$  is at the order of  $O(\|\delta \phi_r\|^4)$ . However,  $\|(K - \hat{\omega}_{r,j}^2 M) \phi_r\|_{M^{-1}}^2$  does not have these properties and so is

not small. Therefore, in the case where  $\phi_r$  is close to  $\phi_r^{\text{Th}}$ , we approximate Eq. (17) using the following equation:

$$\begin{aligned} \log p(\lambda | \hat{\omega}, \hat{\psi}) &= - (1/2) \sum_{r=1}^{N_m} \sum_{j=1}^{N_s} [\{\log(\sigma_r^2) + \|(K - \hat{\omega}_{r,j}^2 M) \phi_r\|_{M^{-1}}^2 / \sigma_r^2\} + \{N_o \log(\delta_r^2) + \|\hat{\psi}_{r,j} - a_r \Gamma \phi_r\|^2 / \delta_r^2\}] \\ &- (1/2) \{\log[\det(P_\rho^0)] + (\rho - \rho^0)^T (P_\rho^0)^{-1} (\rho - \rho^0)\} - (1/2) \{\log[\det(P_\theta^0)] + (\theta - \theta^0)^T (P_\theta^0)^{-1} (\theta - \theta^0)\} + c \quad (22) \end{aligned}$$

## Appendix II. Expectation–Maximization Algorithm

The EM algorithm deals with the problem of probabilistic inference and parameter estimation when some uncertain variables are not observed. The unobserved variable is the system mode shape  $\phi$ , while the parameters we intend to estimate are  $\xi \equiv \{\rho, \theta, a_r, \sigma_r^2, \delta_r^2; r=1 \dots N_m\}$  based on the observed  $\hat{\omega}$  and  $\hat{\psi}$ . Basically, our goal is to find the MPV of  $\xi$

$$\hat{\xi} = \arg \max_{\xi} \log p(\xi | \hat{\omega}, \hat{\psi}) \quad (23)$$

subject to  $A_{\rho} \rho + A_{\theta} \theta < b$ , where

$$\begin{aligned} \log p(\xi|\hat{\omega}, \hat{\psi}) &= \log p(\hat{\omega}, \hat{\psi}|\xi) + \log p(\xi) - \log p(\hat{\omega}, \hat{\psi}) \\ &= \log \int p(\phi, \hat{\omega}, \hat{\psi}|\xi) d\phi + \log p(\xi) - \log p(\hat{\omega}, \hat{\psi}) \end{aligned} \quad (24)$$

However, it is difficult to evaluate  $\log \int p(\phi, \hat{\omega}, \hat{\psi}|\rho, \theta) d\phi$  analytically, and so a direct search for the MPV of  $\xi$  seems blocked.

Let  $q(\phi)$  be any PDF of  $\phi$ , i.e., any non-negative function with

unity integral. Because of the concavity of the logarithm function and Jensen's inequality

$$\begin{aligned} \log \int p(\phi, \hat{\omega}, \hat{\psi}|\xi) d\phi &= \log \int q(\phi) [p(\phi, \hat{\omega}, \hat{\psi}|\xi)/q(\phi)] d\phi \\ &\geq \int q(\phi) \log [p(\phi, \hat{\omega}, \hat{\psi}|\xi)/q(\phi)] d\phi \end{aligned} \quad (25)$$

The last term in Eq. (25) can be further expressed as follows:

$$\begin{aligned} \int q(\phi) \log [p(\phi, \hat{\omega}, \hat{\psi}|\xi)/q(\phi)] d\phi &= \int q(\phi) \log p(\phi, \hat{\omega}, \hat{\psi}|\xi) d\phi - \int q(\phi) \log q(\phi) d\phi = \int q(\phi) \log p(\hat{\omega}, \hat{\psi}|\lambda) d\phi + \int q(\phi) \log p(\phi|\xi) d\phi \\ &\quad - \int q(\phi) \log q(\phi) d\phi = \int q(\phi) \log p(\hat{\omega}, \hat{\psi}|\lambda) d\phi + \int q(\phi) \log p(\phi) d\phi - \int q(\phi) \log q(\phi) d\phi \\ &= \int q(\phi) \log p(\hat{\omega}, \hat{\psi}|\lambda) d\phi + C(q) = E_q[\log p(\hat{\omega}, \hat{\psi}|\lambda)] + C(q) \end{aligned} \quad (26)$$

where  $C(q) = \int q(\phi) \log p(\phi) d\phi - \int q(\phi) \log q(\phi) d\phi$ , and  $E_q[h(\phi)] = \int h(\phi) q(\phi) d\phi$ . In this derivation, we used the fact that  $p(\phi|\xi)$  is not a function of  $\xi$  because for the prior PDF,  $\phi$  and  $\xi$  are independent. Combining Eqs. (24)–(26), we conclude that  $E_q[\log p(\hat{\omega}, \hat{\psi}|\lambda)] + \log p(\xi) - \log p(\hat{\omega}, \hat{\psi}) + C(q)$  is a lower bound of  $\log p(\xi|\hat{\omega}, \hat{\psi})$  for any PDF  $q(\phi)$ . This lower bound depends on  $q(\phi)$  and  $\xi$ , and we denote it by  $L(q, \xi)$ , that is

$$L(q, \xi) \equiv E_q[\log p(\hat{\omega}, \hat{\psi}|\lambda)] + \log p(\xi) - \log p(\hat{\omega}, \hat{\psi}) + C(q) \quad (27)$$

Although it is difficult to optimize  $\log p(\xi|\hat{\omega}, \hat{\psi})$  with respect to  $\xi$  subject to  $A_\rho \rho + A_\theta \theta \leq b$  due to the fact that  $\log \int p(\phi, \hat{\omega}, \hat{\psi}|\xi) d\phi$  is hard to evaluate, it is relatively easy to optimize  $L(q, \xi)$  with respect to  $\xi$  subject to  $A_\rho \rho + A_\theta \theta \leq b$  [later we will show that  $L(q, \xi)$  is quadratic in  $\xi$  so that this optimization is a standard quadratic programming problem].

When  $q(\phi)$  is fixed, the lower bound  $L(q, \xi)$  can be improved by evaluating  $\max_\xi [L(q, \xi)]$ . The values of  $\xi$  that achieve this

maximization subject to  $A_\rho \rho + A_\theta \theta \leq b$  are approximations of the MPV  $\hat{\xi}$ . The quality of this approximation depends the choice of  $q(\phi)$ . The EM algorithm is an algorithm that iteratively chooses a “good”  $q(\phi)$  to improve the estimate of  $\hat{\xi}$ , then, in turn, takes the improved estimate of  $\hat{\xi}$  to find a better  $q(\phi)$ .

The procedure of the EM algorithm can be summarized by the following steps:

1. Initialize  $\xi^{(0)}$  and  $q^{(0)}(\phi)$ .
2. At the  $i$ th iteration: ( $E$  step) From  $\xi^{(i)}$ , derive a good  $q^{(i)}(\phi)$ . Compute  $L[q^{(i)}(\phi), \xi]$ . ( $M$  step) Find  $\xi^{(i+1)} = \arg \max_\xi L[q^{(i)}(\phi), \xi]$  subject to  $A_\rho \rho + A_\theta \theta \leq b$ .
3. Go back to Step 2 for the  $(i+1)$ th iteration and continue cycling until  $\xi^{(i)}$  converge.

Let us first consider the  $E$  step. It is critical to derive a good  $q^{(i)}(\phi)$  from  $\xi^{(i)}$ . A bad choice of  $q^{(i)}(\phi)$  may cause  $L[q^{(i)}(\phi), \xi]$  to be a loose lower bound of  $\log p(\xi|\hat{\omega}, \hat{\psi})$ , and  $\xi^{(i+1)}$  will not be a good approximation for the MPV  $\hat{\xi}$ . On the other hand, if we let  $q^{(i)}(\phi)$  be  $p(\phi|\xi^{(i)}, \hat{\omega}, \hat{\psi})$ , we have

$$\begin{aligned} L[q^{(i)}(\phi), \xi^{(i)}] &= E_{q^{(i)}}[\log p(\hat{\omega}, \hat{\psi}|\phi, \xi^{(i)})] + \log p(\xi^{(i)}) - \log p(\hat{\omega}, \hat{\psi}) + C[q^{(i)}(\phi)] = \int \log p(\hat{\omega}, \hat{\psi}|\phi, \xi^{(i)}) p(\phi|\hat{\omega}, \hat{\psi}, \xi^{(i)}) d\phi + \log p(\xi^{(i)}) \\ &\quad - \log p(\hat{\omega}, \hat{\psi}) + \int p(\phi|\hat{\omega}, \hat{\psi}, \xi^{(i)}) \log p(\phi|\xi^{(i)}) d\phi - \int p(\phi|\hat{\omega}, \hat{\psi}, \xi^{(i)}) \log p(\phi|\hat{\omega}, \hat{\psi}, \xi^{(i)}) d\phi \\ &= \int \log [p(\hat{\omega}, \hat{\psi}|\phi, \xi^{(i)}) p(\phi|\xi^{(i)}) / p(\phi|\hat{\omega}, \hat{\psi}, \xi^{(i)})] p(\phi|\hat{\omega}, \hat{\psi}, \xi^{(i)}) d\phi + \log p(\xi^{(i)}) - \log p(\hat{\omega}, \hat{\psi}) = \int \log p(\hat{\omega}, \hat{\psi}|\xi^{(i)}) p(\phi|\hat{\omega}, \hat{\psi}, \xi^{(i)}) d\phi \\ &\quad + \log p(\xi^{(i)}) - \log p(\hat{\omega}, \hat{\psi}) = \log p(\hat{\omega}, \hat{\psi}|\xi^{(i)}) + \log p(\xi^{(i)}) - \log p(\hat{\omega}, \hat{\psi}) = \log p(\xi^{(i)}|\hat{\omega}, \hat{\psi}) \end{aligned} \quad (28)$$

Therefore, the choice of  $q^{(i)}(\phi)$  being  $p(\phi|\xi^{(i)}, \hat{\omega}, \hat{\psi})$  makes  $L[q^{(i)}(\phi), \xi]$  exactly equal to  $\log p(\xi|\hat{\omega}, \hat{\psi})$  at  $\xi^{(i)}$ , and this is true for all iterations. This choice makes  $\xi^{(i)}$  able to actually converge to the MPV  $\hat{\xi}$ , which maximizes  $\log p(\xi|\hat{\omega}, \hat{\psi})$ .

In order to compute  $L[q^{(i)}(\phi), \xi]$ , we only need to compute the first and second moments of  $q^{(i)}(\phi)$ , i.e.,  $E_{q^{(i)}}(\phi_r)$  and  $E_{q^{(i)}}(\phi_r \phi_r^T)$ ,  $r=1 \dots N_m$ , since

$$\begin{aligned} L[q^{(i)}(\phi), \xi] &= E_{q^{(i)}}[\log p(\hat{\omega}, \hat{\psi}|\lambda)] + \log p(\xi) - \log p(\hat{\omega}, \hat{\psi}) \\ &+ C[q^{(i)}(\phi)] = d - (1/2) \sum_{r=1}^{N_m} \sum_{j=1}^{N_s} [\log(\sigma_r^2) + E_{q^{(i)}}\{\|K\phi_r - \hat{\omega}_{r,j}^2 \cdot M\phi_r\|_{M^{-1}/\sigma_r^2}^2\} + N_o \log(\delta_r^2) + E_{q^{(i)}}\{\|\hat{\psi}_{r,j} - a_r \Gamma \phi_r\|^2/\delta_r^2\}] - (1/2)(\rho \\ &- \rho^0)^T (P_\rho^0)^{-1} (\rho - \rho^0) - (1/2)(\theta - \theta^0)^T (P_\theta^0)^{-1} (\theta - \theta^0) \end{aligned} \quad (29)$$

where  $d$ =quantity not depending on  $\xi$ . Using the fact that for the trace,  $\text{Tr}(AB)=\text{Tr}(BA)$ , we have

$$\begin{aligned} L[q^{(i)}(\phi), \xi] &= d - (1/2) \sum_{r=1}^{N_m} \sum_{j=1}^{N_s} [\log(\sigma_r^2) + E_{q^{(i)}}\{\text{Tr}\{M^{-1}[K\phi_r - \hat{\omega}_{r,j}^2 \cdot M\phi_r][K\phi_r - \hat{\omega}_{r,j}^2 \cdot M\phi_r]^T\}/\sigma_r^2\} + N_o \log(\delta_r^2) + E_{q^{(i)}}\{\text{Tr}\{[\hat{\psi}_{r,j} - a_r \Gamma \phi_r][\hat{\psi}_{r,j} \\ &- a_r \Gamma \phi_r]^T/\delta_r^2\}\}] - (1/2)(\rho - \rho^0)^T (P_\rho^0)^{-1} (\rho - \rho^0) - (1/2)(\theta - \theta^0)^T (P_\theta^0)^{-1} (\theta - \theta^0) = d - (1/2) \sum_{r=1}^{N_m} \sum_{j=1}^{N_s} [\log(\sigma_r^2) + E_{q^{(i)}} \\ &\times \{\text{Tr}\{M^{-1}K\phi_r \phi_r^T K + \hat{\omega}_{r,j}^4 \cdot \phi_r \phi_r^T M - 2\hat{\omega}_{r,j}^2 \cdot M^{-1}K\phi_r \phi_r^T M\}/\sigma_r^2\} + N_o \log(\delta_r^2) + E_{q^{(i)}}\{\text{Tr}\{[\hat{\psi}_{r,j} \hat{\psi}_{r,j}^T + a_r^2 \Gamma \phi_r \phi_r^T \Gamma^T \\ &- 2a_r \Gamma \phi_r \hat{\psi}_{r,j}^T]/\delta_r^2\}\}] - (1/2)(\rho - \rho^0)^T (P_\rho^0)^{-1} (\rho - \rho^0) - (1/2)(\theta - \theta^0)^T (P_\theta^0)^{-1} (\theta - \theta^0) = d - (1/2) \sum_{r=1}^{N_m} \sum_{j=1}^{N_s} [\log(\sigma_r^2) + \text{Tr}\{M^{-1}KE_{q^{(i)}} \\ &\times (\phi_r \phi_r^T)K + \hat{\omega}_{r,j}^4 \cdot E_{q^{(i)}}(\phi_r \phi_r^T)M - 2\hat{\omega}_{r,j}^2 \cdot M^{-1}KE_{q^{(i)}}(\phi_r \phi_r^T)M\}/\sigma_r^2 + N_o \log(\delta_r^2) + \text{Tr}\{[\hat{\psi}_{r,j} \hat{\psi}_{r,j}^T + a_r^2 \Gamma E_{q^{(i)}}(\phi_r \phi_r^T) \Gamma^T - 2a_r \Gamma E_{q^{(i)}} \\ &\times (\phi_r) \hat{\psi}_{r,j}^T]/\delta_r^2\}] - (1/2)(\rho - \rho^0)^T (P_\rho^0)^{-1} (\rho - \rho^0) - (1/2)(\theta - \theta^0)^T (P_\theta^0)^{-1} (\theta - \theta^0) \end{aligned} \quad (30)$$

Moreover,  $E_{q^{(i)}}(\phi_r)$  and  $E_{q^{(i)}}(\phi_r \phi_r^T)$  can be evaluated analytically since  $q^{(i)}(\phi)=p(\phi|\xi^{(i)}, \hat{\omega}, \hat{\psi})$  is a Gaussian PDF of  $\phi$ , which is, in turn, due to the fact that  $\log p(\phi|\xi^{(i)}, \hat{\omega}, \hat{\psi})$  is quadratic in  $\phi$  by our model assumption

$$\begin{aligned} \log p(\phi|\xi^{(i)}, \hat{\omega}, \hat{\psi}) &= d + \log p(\hat{\omega}|\phi, \xi^{(i)}) + \log p(\hat{\psi}|\phi) + \log p(\phi) \\ &= d - (1/2) \sum_{r=1}^{N_m} \sum_{j=1}^{N_s} \{\|K^{(i)}\phi_r - \hat{\omega}_{r,j}^2 M^{(i)}\phi_r\|_{M^{(i)-1}/\sigma_r^{(i)2}}^2 \\ &+ \|\hat{\psi}_{r,j} - a_r^{(i)} \Gamma \phi_r\|^2/\delta_r^{(i)2}\} \end{aligned} \quad (31)$$

The exact values of  $E_{q^{(i)}}(\phi_r)$  and  $E_{q^{(i)}}(\phi_r \phi_r^T)$  are as follows:

$$\begin{aligned} E_{q^{(i)}}(\phi_r) &= E(\phi_r|\xi^{(i)}, \hat{\omega}, \hat{\psi}) = \arg \max \log p(\phi_r|\xi^{(i)}, \hat{\omega}, \hat{\psi}) \\ &= \left[ \sum_{j=1}^{N_s} \{[K^{(i)} - \hat{\omega}_{r,j}^2 M^{(i)}]^T M^{(i)-1} [K^{(i)} - \hat{\omega}_{r,j}^2 M^{(i)}]/\sigma_r^{(i)2} \right. \\ &\left. + a_r^{(i)2} \Gamma^T \Gamma/\delta_r^{(i)2} \right]^{-1} \cdot \left[ \sum_{j=1}^{N_s} a_r^{(i)} \Gamma^T \hat{\psi}_{r,j}/\delta_r^{(i)2} \right] \end{aligned} \quad (32)$$

and

$$\begin{aligned} E_{q^{(i)}}(\phi_r \phi_r^T) &= E(\phi_r \phi_r^T|\xi^{(i)}, \hat{\omega}, \hat{\psi}) = \text{Cov}(\phi_r|\xi^{(i)}, \hat{\omega}, \hat{\psi}) \\ &+ E(\phi_r|\xi^{(i)}, \hat{\omega}, \hat{\psi})E(\phi_r|\xi^{(i)}, \hat{\omega}, \hat{\psi})^T \end{aligned} \quad (33)$$

where

$$\begin{aligned} \text{Cov}(\phi_r|\xi^{(i)}, \hat{\omega}, \hat{\psi}) &= \left[ \sum_{j=1}^{N_s} \{[K^{(i)} - \hat{\omega}_{r,j}^2 M^{(i)}]^T M^{(i)-1} [K^{(i)} \right. \\ &\left. - \hat{\omega}_{r,j}^2 M^{(i)}]/\sigma_r^{(i)2} + a_r^{(i)2} \Gamma^T \Gamma/\delta_r^{(i)2} \right]^{-1} \end{aligned} \quad (34)$$

Now let us consider the  $M$  step. Since  $L[q^{(i)}(\phi), \xi]$  is concave in  $\xi$ , the optimization with respect to  $\xi$  subject to  $A_\rho \rho + A_\theta \theta \leq b$  can be done with global maximization guaranteed. We maximize

$L[q^{(i)}(\phi), \xi]$  using two iterative steps: first with respect to  $\{\sigma_r^2, \delta_r^2: r=1 \dots N_m\}$  with  $\{\rho, \theta, a_r: r=1 \dots N_m\}$  fixed in order to deduce the conditional optimal value  $\{\tilde{\sigma}_r^2, \tilde{\delta}_r^2: r=1 \dots N_m\}$ , and then with respect to  $\{\rho, \theta, a_r: r=1 \dots N_m\}$  with  $\{\tilde{\sigma}_r^2, \tilde{\delta}_r^2: r=1 \dots N_m\}$  substituted into Eq. (30). The first maximization gives

$$\begin{aligned} \tilde{\sigma}_r^2 &= (1/N_s) \sum_{j=1}^{N_s} \text{Tr}\{M^{-1}KE_{q^{(i)}}(\phi_r \phi_r^T)K + \hat{\omega}_{r,j}^4 \cdot E_{q^{(i)}}(\phi_r \phi_r^T)M \\ &- 2\hat{\omega}_{r,j}^2 \cdot M^{-1}KE_{q^{(i)}}(\phi_r \phi_r^T)M\} \end{aligned}$$

$$\begin{aligned} \tilde{\delta}_r^2 &= 1/(N_s N_o) \sum_{j=1}^{N_s} \text{Tr}\{\hat{\psi}_{r,j} \hat{\psi}_{r,j}^T + a_r^2 \Gamma E_{q^{(i)}}(\phi_r \phi_r^T) \Gamma^T - 2a_r \Gamma E_{q^{(i)}} \\ &\times (\phi_r) \hat{\psi}_{r,j}^T\} \end{aligned} \quad (35)$$

The second maximization can be solved by a standard quadratic programming algorithm subject to  $A_\rho \rho + A_\theta \theta \leq b$ . The inner iteration for the  $M$  step stops when satisfactory convergence is achieved with global maximization guaranteed.

We can restate this special EM algorithm, which chooses  $q^{(i)}(\phi)=p(\phi|\xi^{(i)}, \hat{\omega}, \hat{\psi})$ , as follows:

1. Initialize  $\xi^{(0)}$  and  $q^{(0)}(\phi)$ .
2. At the  $i$ th iteration: ( $E$  step): Compute the first and second moments  $E_{q^{(i)}}(\phi_r)$  and  $E_{q^{(i)}}(\phi_r \phi_r^T)$ ,  $r=1 \dots N_m$ , and substitute them into Eq. (30) to compute  $L[q^{(i)}(\phi), \xi]$  analytically. ( $M$  step): Solve the concave optimization problem  $\xi^{(i+1)} = \arg \max_\xi L[q^{(i)}(\phi), \xi]$  subject to  $A_\rho \rho + A_\theta \theta \leq b$  by an inner iteration with the following steps:
  - Fix  $\{\rho, \theta, a_r: r=1 \dots N_m\}$ , optimize  $L[q^{(i)}(\phi), \xi]$  with respect to  $\{\sigma_r^2, \delta_r^2: r=1 \dots N_m\}$ .
  - Fix  $\{\sigma_r^2, \delta_r^2: r=1 \dots N_m\}$ , optimize  $L[q^{(i)}(\phi), \xi]$  with respect to  $\{\rho, \theta, a_r: r=1 \dots N_m\}$ .
  - Go back to Step 2(1) until convergence of the inner iteration.

3. Go back to Step 2 for the  $(i+1)$ th iteration and continue cycling until  $\xi^{(i)}$  converge.

After convergence to satisfactory accuracy,  $\hat{\xi}$  is found, and  $\hat{\phi}$  is simply the first moment of  $p(\phi|\hat{\xi}, \hat{\omega}, \hat{\psi})$  since

$$p(\phi, \hat{\xi}|\hat{\omega}, \hat{\psi}) = p(\phi|\hat{\xi}, \hat{\omega}, \hat{\psi})p(\hat{\xi}|\hat{\omega}, \hat{\psi}) \quad (36)$$

and so

$$\begin{aligned} \hat{\phi} &= \arg \max p(\phi, \hat{\xi}|\hat{\omega}, \hat{\psi}) = \arg \max p(\phi|\hat{\xi}, \hat{\omega}, \hat{\psi})p(\hat{\xi}|\hat{\omega}, \hat{\psi}) \\ &= \arg \max p(\phi|\hat{\xi}, \hat{\omega}, \hat{\psi}) = E(\phi|\hat{\xi}, \hat{\omega}, \hat{\psi}) \end{aligned} \quad (37)$$

The last equality in Eq. (37) is due to the fact that  $p(\phi|\hat{\xi}, \hat{\omega}, \hat{\psi})$  is Gaussian. We call this special EM algorithm the tight EM (TEM) algorithm since a tight lower bound of  $\log p(\xi|\hat{\omega}, \hat{\psi})$  is achieved for each iteration. The TEM algorithm is an ascent optimization algorithm for  $\log p(\xi|\hat{\omega}, \hat{\psi})$ , i.e.,  $\log p(\xi^{(i)}|\hat{\omega}, \hat{\psi})$  always increases during iterations. Indeed, during the  $M$  step, we let

$$\xi^{(i+1)} = \arg \max_{\xi} L[q^{(i)}(\phi), \xi] \quad (38)$$

and therefore

$$L[q^{(i)}(\phi), \xi^{(i+1)}] \geq L[q^{(i)}(\phi), \xi^{(i)}] = \log p(\xi^{(i)}|\hat{\omega}, \hat{\psi}) \quad (39)$$

Furthermore, after the next  $E$  step

$$\begin{aligned} \log p(\xi^{(i+1)}|\hat{\omega}, \hat{\psi}) &= L[q^{(i+1)}(\phi), \xi^{(i+1)}] = \max_q L[q, \xi^{(i+1)}] \\ &\geq L[q^{(i)}(\phi), \xi^{(i+1)}] = \log p(\xi^{(i)}|\hat{\omega}, \hat{\psi}) \end{aligned} \quad (40)$$

## References

- Beck, J. L. (1978). "Determining models of structures from earthquake records." Technical Rep. EERL 78-01, Earthquake Engineering Research Laboratory, California Institute of Technology, Pasadena, Calif. (<http://caltecheerl.library.caltech.edu/archive/00000183/>)
- Beck, J. L. (1996). "System identification methods applied to measured seismic response." *Proc., 11th World Conf. Earthquake Engineering*, Acapulco, Mexico.
- Beck, J. L., Au, S. K., and Vanik, M. W. (2001). "Monitoring structural health using a probabilistic measure." *Comput. Aided Civ. Infrastruct. Eng.*, 16, 1–11.
- Beck, J. L., and Katafygiotis, L. S. (1998). "Updating models and their uncertainties. Part I: Bayesian statistical framework." *J. Eng. Mech.*, 124(4), 455–461.
- Beck, J. L., May, B. S., and Polidori, D. C. (1994). "Determination of modal parameters from ambient vibration data for structural health monitoring." *Proc., 1st World Conf. on Structural Control*, Pasadena, Calif., TA3:3–TA3:12.
- Bernal, D. (2002). "Load vectors for damage localization." *J. Eng. Mech.*, 128(1), 7–14.
- Bernal, D., Dyke, S. J., Beck, J. L., and Lam, H. F. (2002). "Phase II of the ASCE benchmark study on structural health monitoring." *Proc., 15th Engineering Mechanics Division Conf.*, ASCE, Reston, Va.
- Casciati, F., ed. (2002). *Proc., 3rd World Conf. on Structural Control*, Como, Italy.
- Chang, F. K., ed. (2001). *Proc., of 3rd Int. Workshop on Structural Health Monitoring*, Stanford, Calif.
- Ching, J., and Beck, J. L. (2003c). "Detecting beam-column connection failures in ASCE Phase II simulated benchmark studies using a two-step Bayesian structural health monitoring approach." *Proc., 9th Int. Conf. on Applications of Statistics and Probability in Civil Engineering*, San Francisco.
- Ching, J., and Beck, J. L. (2003b). "Two-stage Bayesian structural health monitoring approach for Phase II ASCE benchmark studies." *Proc., 21st Int. Modal Analysis Conf.*, Orlando, Fla.
- Ching, J., and Beck, J. L. (2003a). "Two-step Bayesian structural health monitoring approach for IASC–ASCE Phase II simulated and experimental benchmark studies." Technical Rep. No. EERL 2003-02, Earthquake Engineering Research Laboratory, California Institute of Technology, Pasadena, Calif. (<http://caltecheerl.library.caltech.edu/archive/00000352/>)
- Cox, R. T. (1961). *The algebra of probable inference*, Johns Hopkins University Press, Baltimore.
- Dyke, S. J. (1999). (<http://wusceel.cive.wustl.wustl.edu/asce.shm/benchmarks.htm>)
- Dyke, S. J., Bernal, D., Beck, J. L., and Ventura, C. (2001). "An experimental benchmark problem in structural health monitoring." *Proc., 3rd Int. Workshop on Structural Health Monitoring*, Stanford, Calif.
- Dyke, S. J., Bernal, D., Beck, J. L., and Ventura, C. (2003). "Experimental phase of the structural health monitoring benchmark problem." *Proc., 16th Engineering Mechanics Conf.*, ASCE, Reston, Va.
- Hjelmstad, K. D., and Shin, S. (1997). "Damage detection and assessment of structures from static response." *J. Eng. Mech.*, 123(6), 568–576.
- Jaynes, E. T. (1957). "Information theory and statistical mechanics." *Phys. Rev.* 106, 620–630.
- Johnson, E. A., Lam, H. F., Katafygiotis, L. S., and Beck, J. L. (2004). "Phase I IASC–ASCE structural health monitoring benchmark problem using simulated data." *J. Eng. Mech.*, 130(1), 3–15.
- Natke, H. G., and Yao, J. T. P., eds. (1988). *Proc., Workshop on Structural Safety Evaluation Based on System Identification Approaches*, Vieweg, Wiesbaden, Germany.
- Papadimitriou, C., Beck, J. L., and Katafygiotis, L. S. (1997). "Asymptotic expansions for reliabilities and moments of uncertain dynamic systems." *J. Eng. Mech.*, 123(12), 1219–1229.
- Rosenkrantz, R. D., ed. (1982). *E. T. Jaynes: Papers on probability, statistics and statistical physics*, Reidel, Dordrecht, Holland.
- Sanayei, M., McClain, J. A. S., Wadia-Fascetti, S., and Santini, E. M. (1999). "Parameter estimation incorporating modal data and boundary conditions." *J. Struct. Eng.*, 125(9), 1048–1055.
- Shumway, R. H., and Stoffer, D. S. (1982). "An approach to time series smoothing and forecasting using the EM algorithm." *J. Time Ser. Anal.*, 4, 253–263.
- Vanik, M. W. (1997). "A Bayesian probabilistic approach to structural health monitoring." Technical Rep. No. EERL 97-07, Earthquake Engineering Research Laboratory, California Institute of Technology, Pasadena, Calif. (<http://caltecheerl.library.caltech.edu/archive/00000049/>)
- Vanik, M. W., Beck, J. L., and Au, S. K. (2000). "Bayesian probabilistic approach to structural health monitoring." *J. Eng. Mech.*, 126(7), 738–745.
- Yuen, K. V., Au, S. K., and Beck, J. L. (2004). "Two-stage structural health monitoring approach for Phase I benchmark studies." *J. Eng. Mech.*, 130(1), 16–33.